Effect of Temperature on the Lattice Strain Evolution in a Textured Alpha Titanium: Neutron Diffraction and Modelling

Kodjo Emmanuel Agbovi, Baptiste Girault, Jamal Fajoui, Saurabh Kabra, Winfried Kockelmann, Pierre-Antoine Dubos, David Gloaguen

Effect of temperature on the lattice strain evolution in a textured alpha titanium: neutron diffraction and modelling

Kodjo Emmanuel Agbovi[1], Baptiste Girault[1], Jamal Fajoui[1], Saurabh Kabra[2], Winfried Kockelmann[2], Pierre-Antoine Dubos[1], David Gloaguen[1*]

[1] Nantes Université, Ecole Centrale Nantes, CNRS, GeM, UMR 6183, F-44600 Saint-Nazaire, France
[2] ISIS Neutron and Muon Source, Science and Technology Facilities Council (SFTC), Rutherford Appleton Laboratory, Harwell, OX11 0QX, United Kingdom
[*] Corresponding author: david.gloaguen@univ-nantes.fr

Abstract

Plastic deformation of titanium alloys depends on the temperature and the mechanical loading mode. It is accommodated by a complex mixture of slip and twinning systems. It remains nevertheless unclear which deformation modes are activated in the polycrystal during loading, especially with the temperature. In order to better understand the mechanical behaviour of textured α-Ti, neutron diffraction measurements have been performed to analyse the intergranular strain evolution under tensile tests at different temperatures ranging from ambient up to 300°C. The material has then been characterized from meso- (grain) to macroscopic scales in order to obtain relevant information about the deformation mechanisms governing its global behaviour. An elastoplastic self-consistent approach has been used to explain and interpret the experimental observations achieved under thermomechanical loadings. The model has enabled us to successfully predict the measured macroscopic behaviour and the lattice strain development. The study has also provided a comprehensive data set and a complete description of temperature influence onto the mechanical state and the plastic anisotropy, especially at the mesoscopic level. The evolution of the deformation mode hierarchy and the internal stress fields with the temperature have been determined.

Keywords: diffraction, lattice strains, plasticity, temperature, model, titanium

1. Introduction

Plastic anisotropy, crystallographic texture and temperature greatly affect the mechanical behaviour, at different scales, of α-titanium (α-Ti), with a Hexagonal Close Packed (HCP) crystalline structure [1]. The mechanisms governing the plasticity of HCP materials, in particular α-Ti, are historically less studied and more complex than those of cubic alloys. The strong plastic anisotropy of HCP materials is due to the fact that they do not have as many easily activated slip systems as metallic alloys do with a cubic structure. It is induced by slip on several plane families depending on the loading conditions and microstructural characteristics. Plasticity in this type of alloy can also be induced by twinning which is an important deformation mode allowing the accommodation of plasticity along the $\vec{c}$-axis. Depending on the temperature and the loading mode, plasticity in α-Ti displays a complex sequence of activation of these different deformation modes. The identification of the activated systems and their hierarchy, especially with temperature, are not yet clear.

Further experimental investigations have shown that the active deformation mechanisms in titanium vary with temperature. The prismatic slip $\{10.0\}\langle 11.0\rangle$ is the main deformation mode of α-Ti over a large temperature range (77–1073 K) [2–4]. Secondary slip modes such as basal slip $\{00.2\}\langle 11.0\rangle$ and pyramidal $\langle a\rangle$ slip $\{10.1\}\langle 11.0\rangle$ are then potential candidates for higher temperatures [3,5]. To accommodate the deformation along the $\vec{c}$-axis, the activation of pyramidal $\langle c+a\rangle$ slip $\{10.1\}\langle 11.3\rangle$ is generally necessary [1,6]. The activity of the twinning becomes less important as the temperature is increasing [7]. This decrease in the activity of the twinning modes is then compensated by a greater activity of the secondary slip modes (basal and

pyramidal). Recently, Fu *et al.* [8] have studied deformation mechanisms of commercially pure titanium under biaxial loading at ambient and elevated temperatures by transmission electron microscopy. Their results confirm these general trends previously detailed. However, it is difficult to establish a clear hierarchy between them since this depends on many factors such as the loading mode and the strain rate [9], the grain size [10], the crystallographic texture [11], the chemical composition [12] and the temperature [9,13]. Moreover, most of the results in the literature come from studies on single-crystals [2,12,14–16]. There are currently too few data available on polycrystals to obtain an accurate understanding of how the temperature affects the deformation mechanisms involved in titanium alloys [17,18]. More precisely, CRSS (Critical Resolved Shear Stress) values and its evolution with temperature have largely remained unknown and the available data have been obtained mainly on single-crystals [19].

Neutron diffraction is a non-destructive technique which is able to characterise the distribution of internal stresses/elastic strains and thus to better understand the role played by the different deformation mechanisms responsible for their development. Diffraction technique provides valuable and complex information on the stresses undergone by the material at the scale of the diffracting volume and on the behaviour of the polycrystalline aggregate at an intermediate scale between the macroscopic and microscopic scales [20–22].

This technique is a relevant tool to provide the necessary data for the development of models based on a micromechanical approach like the mean field models and also allows to validate them. In turn, these approaches are necessary to correctly interpret the experimental data obtained [23–26]. This methodology has been applied to study the plasticity of titanium alloys at room temperature [24,27–33]. It should be noted that there are very few studies using this coupling to study the plasticity of HCP materials with temperature in the existing literature. Oliver *et al.* [34] have studied the intergranular strain development in IMI 125, a commercially pure titanium, by

neutron diffraction during uniaxial loading at room temperature and 200°C. An elastoplastic self-consistent approach was used to interpret neutron data and obtain some information on the active deformation modes. The intergranular strain developments during tension at 200°C show the same trend than those from room temperature. $\{10.2\}\langle\bar{1}0.0\rangle$ twinning seems to have a contribution that decreases with increasing temperature. Neutron experiments were performed with only 3 plane families and the comparison with the model was made for one high temperature. The discrepancies observed by the authors at 200°C are explained by the assumption of the model: isotropic hardening law and twinning modelled like a directional slip system. Lee *et al.* [35] investigated experimentally the anisotropic lattice behaviour of Grade 2 CP-Ti by using *in situ* tensile testing under neutron diffraction combined with EBSD measurements at temperatures of 15–298 K. The authors highlighted that the deviation of linearity in the lattice strains was caused by the load-redistribution between plastically soft and hard grain families, resulting in the three-stage hardening behaviour. Twinning activity was more active at lower temperature. Nevertheless, no information is available on the evolution in the hierarchy of the deformation modes because of the lack of a scale transition model.

Studies on zirconium alloys can be cited since, as titanium alloys do, they activate prismatic slip as the main deformation mode. For example, Li *et al.* [36] investigated the tensile behaviour of samples from a cold rolled plate of Zircaloy-4, at Room Temperature (RT) and 250°C. The mechanical response of the prismatic {10.0}, basal {00.2} and pyramidal {10.1} planes families was predicted using an Elasto-Plastic Self-Consistent (EPSC) approach. A good agreement was found between the modelling and the experiment results in terms of macroscopic stress-strain and internal strain evolution at RT.

Evans *et al.* [37] used the same type of alloy for synchrotron X-ray diffraction measurements during *in situ* tensile and compression tests at high temperature (≈ 550°C). They were able to

correctly predict the evolution of the experimentally observed stress fields and crystallographic texture via an EPSC model originally developed by Turner *et al.* [33] and Clausen *et al.* [38,39]. They found that twinning is facilitated at high strain rates (10^{-1} to 10^{-2} s^{-1}) and its activity is decreasing with decreasing rate. At 550°C and low strain rates (10^{-4} s^{-1}), pyramidal slip ⟨c + a⟩ is the main deformation mode followed by pyramidal slip ⟨a⟩ and prismatic slip.

In a previous work, a coupled neutron diffraction and polycrystalline modelling approach has been used to study intergranular strain in an α-Ti alloy during tensile loadings at RT [31]. Because of the current lack of data on plasticity of titanium alloys with temperature, it is interesting to extend this study to different temperatures (with the same material). The objective of this work is thus to compare the mechanical behaviour of a commercially pure α-titanium at RT, 100 and 300°C under uniaxial tensile loading. Neutron diffraction results have been compared with those obtained from a modified self-consistent model to determine the evolution in the hierarchy of the deformation modes, the CRSS values and the internal stress fields with the temperature. The model considers grain reorientation and stress relaxation induced by twinning activity. To understand how internal strains evolve, a consistent set of data (i.e. 8 {hk.l} grain families measured along both loading and transverse directions for 9 macroscopic pre-strains) that characterises the behaviour of a grain group from a representative volume has been selected. Our study may serve as a contribution to this general effort to understand and clarify the physical mechanisms involved in the plastic deformation of titanium alloys with temperature.

2. Experimental details

2.1.Material

The experimental material is an extruded rod of titanium alloy (Commercially Pure α-titanium, denoted CP α -Ti, Ti + 0.614 wt.%Fe + 0,137 wt.%O + 0.012 wt.%C + 0.0078 wt.%N) with an average grain size of about 45 μm. Tensile cylindrical specimens with a gauge part of 8 mm in diameter and 42 mm in length were machined along the extrusion direction (represented by the Longitudinal Direction, LD) for neutron diffraction experiments. In order to analyse the crystallographic texture, the GEM (GEneral Materials diffractometer) instrument has been used at ISIS, UK. Pole Figures (PFs) for the as-received material, shown in Figure 1.a, were calculated using the E-WIMV algorithm implemented in the MAUD program package [40]. Information about the instrument and the measurement technique can be found in Refs. [41,42]. The studied material displays an asymmetrical texture with the majority of the grains having the basal {00.2} plane-normals located in the Transverse Direction (TD)-Normal Direction (ND) plane, close to the transverse direction TD (with a maximum of 7.2 mrd located at about 15° from TD) and thus perpendicular to the longitudinal direction LD (i.e. the extrusion direction) (Figure 1.a). The {10.0} pole figure shows a slight reinforcement at large values of ψ, especially along the LD.

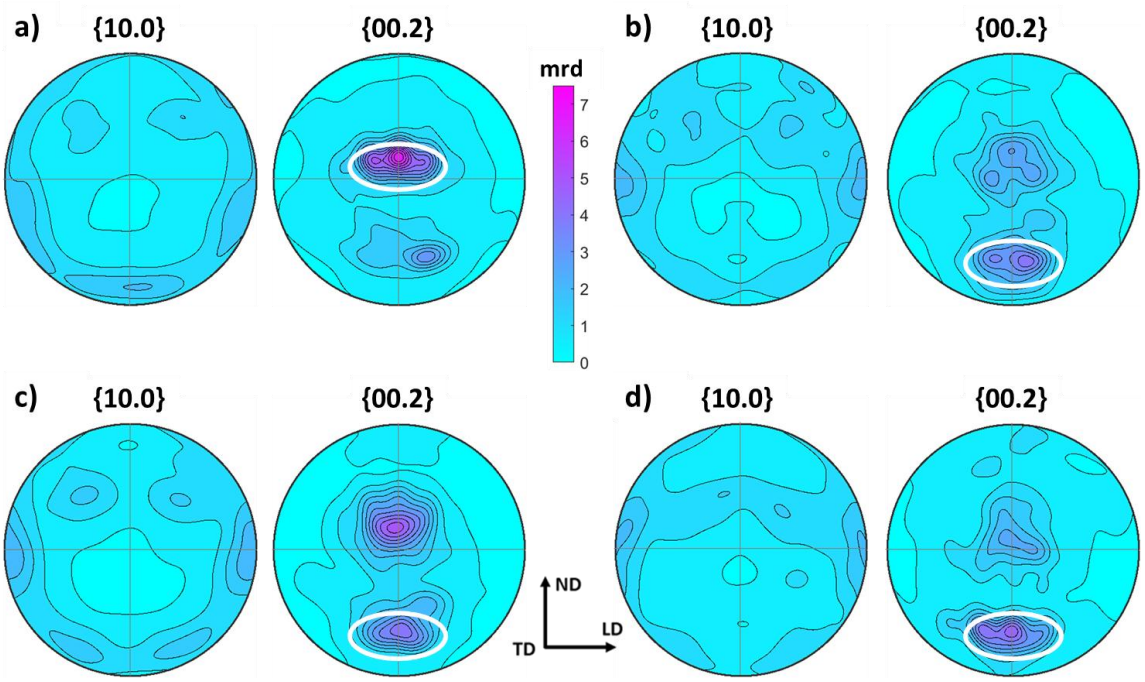

Figure 1: crystallographic textures of the studied specimens. As-received samples (a), after the tensile loading up to 6 %: at room temperature (b), at 100°C (c) and at 300°C (d). {10.0} and {00.2} PFs are represented in the LD-ND plane. ND: Normal Direction, TD: Transverse Direction, LD: Longitudinal Direction.

2.2.Neutron diffraction tests

The samples were tested at the stress/strain diffractometer ENGIN-X at the ISIS time-of-flight neutron source (Didcot, Oxfordshire, UK) [43] at RT, 100°C and 300°C using a 50 kN Instron testing machine with a strain rate of 10^{-5} s^{-1} up to 6 % of macroscopic strain. Temperatures of 100 and 300°C were reached at rates of 10 and 20°C per minute, respectively, and measured with a K-type thermocouple. Before each mechanical test, temperatures were kept constant for 30 to 45 minutes to ensure the temperature stability. The loading axis has been set at 45° from the incident neutron beam. The two detector banks, located at ± 90° form the incident beam have enabled the

simultaneous collection of diffraction spectra (effective d-spacing ranging from 0.88 to 2.63 Å) with scattering vectors axially ($\vec{Q}_{//}$) and radially ($\vec{Q}_{\perp}$) aligned to the loading axis. The irradiated gauge volume is a cube ($4 \times 4 \times 4$ mm^3) resulting from the crossing of the incident and diffracted beams and defined by the vertical and horizontal collimation slits. A counting time of 43 min per measurement has been chosen.

The lattice strain $\langle \varepsilon(hk.l,\varphi,\psi)\rangle_{V_d}$ of a grain group having a shared {hk.l} plane-normal parallel to the diffraction vector $\vec{Q}$ (defined by azimuthal and inclination angles, respectively φ and ψ) can be determined by:

$$\langle \varepsilon(hk.l,\varphi,\psi)\rangle_{V_d} = ln\left(\frac{\langle d(hk.l,\varphi,\psi)\rangle_{V_d}}{d_0(hk.l)}\right) \quad (1)$$

$\langle\ \rangle_{V_d}$ indicates an averaging over diffracting grains for a given {hk.l} reflection. $\langle d(hk.l,\varphi,\psi)\rangle_{V_d}$ is the measured lattice plane spacing of the hkl diffraction peak. Resulting lattice strain values are given as micro-strain (denoted με, i.e. units of 10^{-6}). $d_0(hk.l)$ is the lattice plane spacing prior to mechanical loading. Single peak fitting was performed using the Open Genie code [44] with Gaussian function. The fitting algorithm also provides an estimate of the statistical error of the peak position, which determines the statistical error of the strain measurement.

Neutron measurements are characterized by a relatively long acquisition time. To avoid any strain relaxation due to the creep behaviour during data collection, even at RT, the sample was first deformed to the desired macroscopic strain and then immediately unloaded, as shown in Figure 2. Successive steps have been achieved at RT, 100 and 300°C in the plastic regime, enabling the study of the remaining residual strains at zero applied load, resulting from a given

increment of plastic deformation. This approach permits to avoid that lattice strains evolve during the measurement.

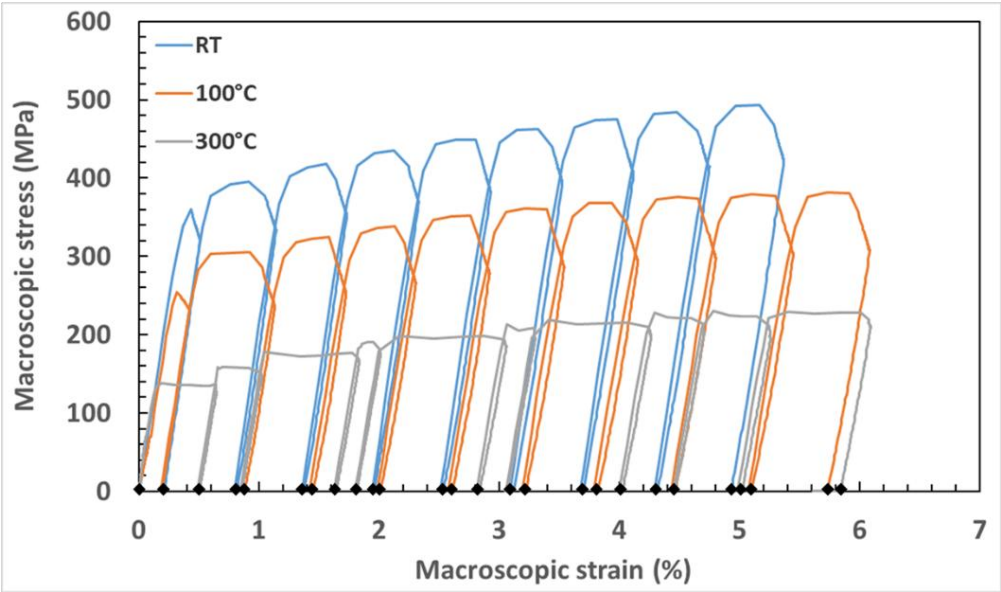

Figure 2: Experimental macroscopic stress-strain curves at RT, 100 and 300°C. The black points indicate the macroscopic strain during neutron measurements after unloading, i.e. at zero applied load.

Figure 1 shows the crystallographic texture after the mechanical test for each temperature and latter is compared to the initial one. Before the test, most of the grains, as previously indicated, have their basal normal close to the transverse direction with a maximum located at about 15° from TD and perpendicular to the loading direction (i.e. LD). After a total macroscopic strain of about 6 % (Figure 1.b), a reorientation of the {00.2} poles (white framed area) is observed. It can be explained by the activation of $\{11.2\}\langle 11.\bar{3}\rangle$ compression twinning that induces a reorientation of the basal poles of about 65° [45,46]. Tensile loading along the LD produces a $\vec{c}$-axis reorientation for grains suitably orientated for this type of twinning. Similar observations can be

reported for the samples deformed at 100°C (Figure 1.c) and 300°C (Figure 1.d) as regard to compression twinning activation. The twinned volume fraction can be determined focusing on the intensity difference observed between {00.2} PFs before (as-received) and after plastic deformation. Based on the previous work of Brown *et al.* [47] and integrating over a sub-space associated to the twin component (represented by the white framed area in Figure 1.a), the total twin volume fractions after 6 % applied macroscopic strain are about 13, 6.2 and 5.3 % at RT, 100 and 300°C, respectively.

3. Elastic–plastic self-consistent model and material parameters

The different macroscopic stress–strain curves and the results of neutron diffraction experiments performed in this study were modelled using an EPSC approach. All the information concerning the developed EPSC algorithm used in this work can be found in [48]. Agbovi *et al.* [22] have recently proposed an extended EPSC code with the implementation of a twinning scheme into the original model. The current EPSC model accounts for (i) the texture evolution due to the reorientation of the parent grains during twinning events, (ii) the local stress relaxation due to twinning and, (iii) the twinning fraction effect on texture changes.

The material is assumed to consist of an agglomerate of single-crystals. Each of them is defined by a crystallographic orientation described by a set of Euler angles weighted to reproduce the initial crystallographic texture. In this approach, each single-crystal is treated as an ellipsoidal inclusion, with a given crystallographic orientation, embedded in a Homogeneous Equivalent Medium (HEM) representing the average properties of the textured polycristal. In order to predict the stress/strain state of the grain under a mechanical load, elastic constant tensor (and subsequent

anisotropy), crystallographic slip/twinning directions and planes are assigned to each grain. A hardening matrix H^{gh} is introduced to describe the evolution of the Critical Resolved Shear Stress (CRSS) with strain for each deformation mode g, as a function of the plastic slip (or twinning) on the other deformation systems h:

$$\dot{\tau}_c^g = \sum_h H^{gh}\dot{\gamma}^h \quad (2)$$

$\dot{\gamma}^h$ is the slip rate on the h-th active system.

The hardening matrix is described as follow [53]:

$$H^{gh} = qH^{gg} \ (g \neq h) \quad (3)$$

H^{gg} is the self-hardening coefficient and H^{gh} corresponds to the latent hardening when g system is different from h. The q factor defines the degree of latent hardening.

When samples are heated prior to the mechanical test, each grain undergoes an expansion depending on its crystallographic orientation due to the thermal expansion anisotropy. When the temperature is increased from RT to 100 or 300°C, internal elastic strains, resulting from the interaction between the grains, appear in the polycrystal and thus generate internal stresses. A thermoelastic formulation has been used to simulate the evolution of thermal stresses associated to the heating at 100 and 300°C [54]. The EPSC scheme is then used to predict the mechanical behaviour of titanium polycrystal under a uniaxial tension for a given temperature. Since elastic (c_{ij}) and thermal (α_{ij}) coefficients depend on temperature, their evolution with temperature was taken into account through the measurements achieved by Fisher and Renken [55] and Wasilewski [56], respectively. The temperature dependence of these coefficients can be described by a polynomial relation given in [54].

The initial texture input for simulations is represented by a discrete distribution of 2000 spherical grains with Euler angle orientations weighted according to the Crystallographic Orientation

Distribution Function (CODF). These orientations are generated through a discretisation process with the algorithm proposed by Toth and Van Houtte [57]. The amount of crystallites has been chosen in order to provide a true picture of the polycrystalline aggregate and is the result of a specific numerical study (achieved to faithfully reproduce the overall macroscopic stress-strain curve as well as lattice strain).

The thermal and elastic properties of titanium single-crystal at room temperature are listed in Table I. The elastic constants of titanium single-crystal used in the model at 100 and 300°C were obtained by the polynomial relations given in [54].

α_{11} (= α_{22})	α_{33}	c_{11}	c_{33}	c_{44}	c_{12}	c_{13}
9.9	12.0	162.4	180.7	46.7	92.0	69.0

Table I: Thermal expansion coefficients ($\times 10^{-6}\ K^{-1}$) [56] *and elastic constants (GPa)* [58] *at single-crystal scale and at RT.*

Based on the previous studies presented in the introduction, the following deformation modes were implemented in the present EPSC simulations for the range of temperatures studied: prismatic slip $P\langle a\rangle : \{10.0\}\langle 11.0\rangle$, basal $B\langle a\rangle : \{00.1\}\langle 11.0\rangle$, pyramidal $\Pi_1\langle a\rangle : \{10.1\}\langle 11.0\rangle$, first-order pyramidal $\Pi_1\langle c + a\rangle : \{10.1\}\langle 11.3\rangle$ and $\{11.2\}$ twinning (ctw-$\{11.2\}$).

To determine the model parameters (CRSS and hardening coefficients), a method akin to the one developed by [31] has been used in the present work. Briefly, initial values of CRSS and hardening parameters have been determined adjusting the model results to the experimental neutron diffraction data and macroscopic stress–strain responses. To define the interactions between the deformation systems, the term defining the latent hardening, q (equations 2 and 3), is

set to a value of 1.3 in order to provide the best accordance between the predicted and experimental results.

In order to obtain the final material parameters from neutron strain measurements, a least squares method is used, for each temperature, to optimize the different parameters by minimizing a function e^2 defined as the sum of squares between deviations of the experimental and simulated quantities, over all *n* grain groups:

$$e^2 = \sum_{i=1}^{n} \left(\frac{\langle \varepsilon(hk.l,\varphi,\psi)\rangle^{i}_{V_{d\ meas}} - \langle \varepsilon(hk.l,\varphi,\psi)\rangle^{i}_{V_{d\ simul}}}{u\left(\langle \varepsilon(hk.l,\varphi,\psi)\rangle^{i}_{V_{d\ meas}}\right)} \right)^2 \quad (4)$$

where $\langle \varepsilon(hk.l,\varphi,\psi)\rangle^{i}_{V_{d\ meas}}$ is the measured value, $\langle \varepsilon(hk.l,\varphi,\psi)\rangle^{i}_{V_{d\ simul}}$, the simulated value, and $u\left(\langle \varepsilon(hk.l,\varphi,\psi)\rangle^{i}_{V_{d\ meas}}\right)$, the uncertainty associated to the measured lattice strain.

The final set of material parameter values giving the best agreement between the simulated and the measured results is summarized in Table II.

Temperature	**RT**		**100 C**		**300 C**	
system	$\boldsymbol{\tau_c}$	**H**	$\boldsymbol{\tau_c}$	**H**	$\boldsymbol{\tau_c}$	**H**
P⟨a⟩	115 (1)	120	90 (1)	100	42 (1)	50
B⟨a⟩	150 (1.30)	180	110 (1.22)	140	45 (1.07)	70
$\boldsymbol{\Pi_1\langle a\rangle}$	130 (1.13)	140	100 (1.11)	120	50 (1.19)	90
$\boldsymbol{\Pi_1\langle c+a\rangle}$	240 (2.09)	250	180 (2)	210	120 (2.86)	150
ctw-{11.2}	250 (2.17)	300	200 (2.22)	230	170 (4.05)	220

Table II: CRSS and hardening coefficients (MPa) at RT, 100 and 300 C. In blue, normalized CRSS values with respect to $CRSS^{\boldsymbol{P\langle a\rangle}}$*, determined with the EPSC modelling of the neutron diffraction results.*

4. Experimental and modelling results

The macroscopic stress-strain curves at RT, 100 and 300°C are shown in Figure 3. The EPSC approach correctly reproduces the experimental curves for the three studied temperatures. The plastic slopes predicted by the model agree with the experiments up to 6 % total strain. The model captures the observed flow curve with an excellent agreement. The calculated Young's moduli coincide well with the experimental ones (Table III).

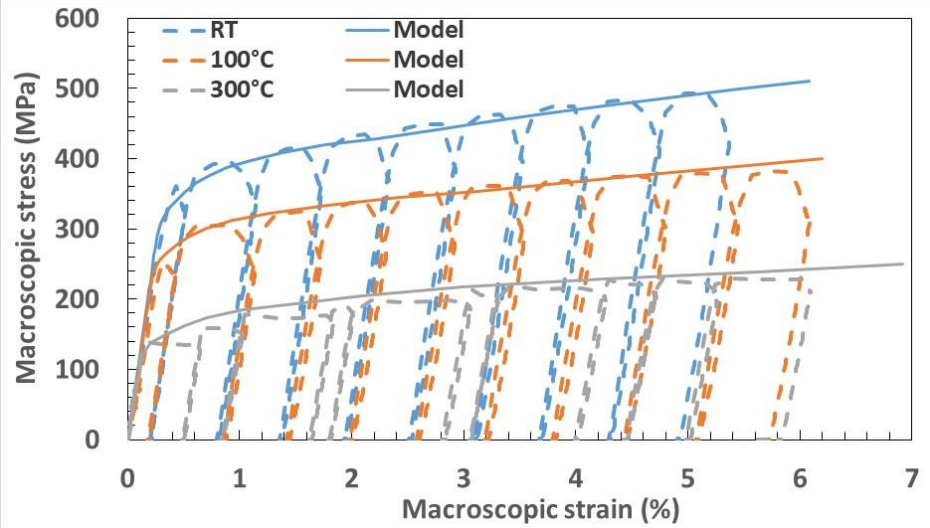

Figure 3: Experimental (dashed lines) and predicted (solid lines) macroscopic stress - strain curves for RT (blue), 100 (orange) and 300°C (grey).

Temperature	experimental	simulated
RT	102 ± 1	107
100°C	95 ± 2	101
300°C	91 ± 2	89,9

Table III: Experimental and simulated Young's moduli (GPa) for the different studied temperatures.

The simulations reveal that the contribution of the activated deformation mechanisms differs with temperature: RT (Figure 4.a), 100 (Figure 4.b) and 300°C (Figure 4.c). Plasticity is initiated at an applied stress of 263 MPa (0.24 % macroscopic strain) at RT, 212 MPa (0.2 % macroscopic strain) at 100°C and 108 MPa (0.12 % macroscopic strain) at 300 °C. Prismatic slip remains the main deformation system during plastic deformation no matter the considered temperature. However, among the activated slip systems, the contribution of basal slip remains minor with a percentage always set below 20 %.

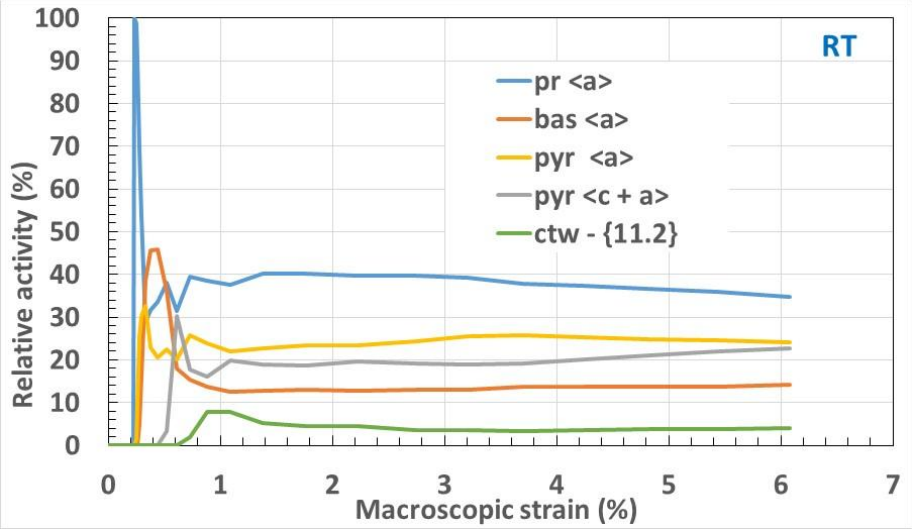

(a)

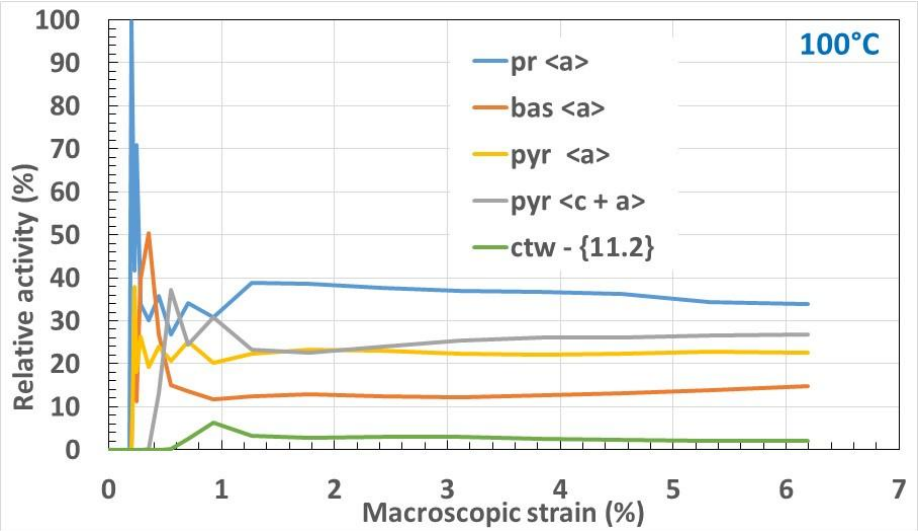

(b)

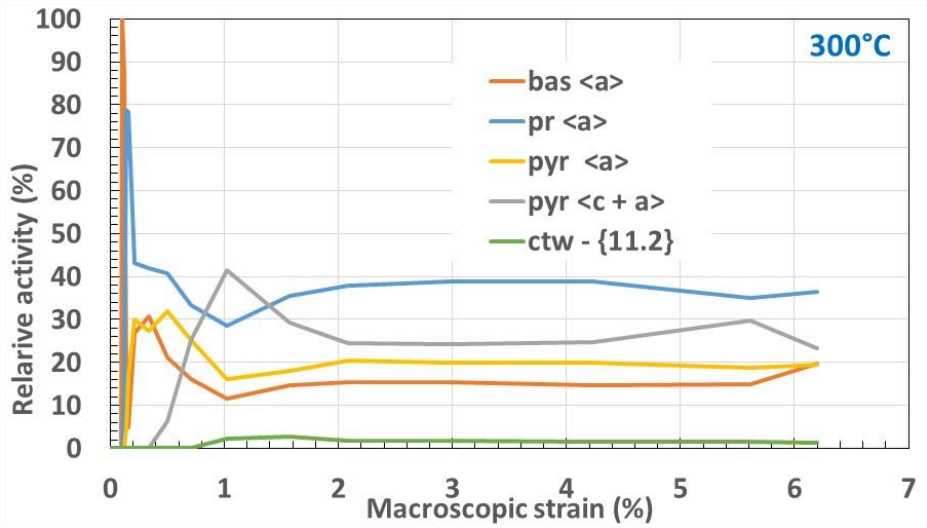

(c)

Figure 4: Relative activity of the slip and twin modes to the total plastic deformation as a function of the macroscopic strain at (a) RT, (b) 100 and (c) 300°C.

In this section, the experimental data will be compared with the predicted results. The measured (symbol) and simulated (solid line) intergranular residual elastic strains, after elastic unloading,

for the 8 {hk.l} grain families studied during the tensile tests are presented in Figure 5 for RT, in Figure 6 for 100°C and in Figure 7 for 300°C.

The residual strains along (i.e. longitudinal) and perpendicular (i.e. transverse) to the loading direction (extrusion direction) are referenced by the symbols // and ⊥.

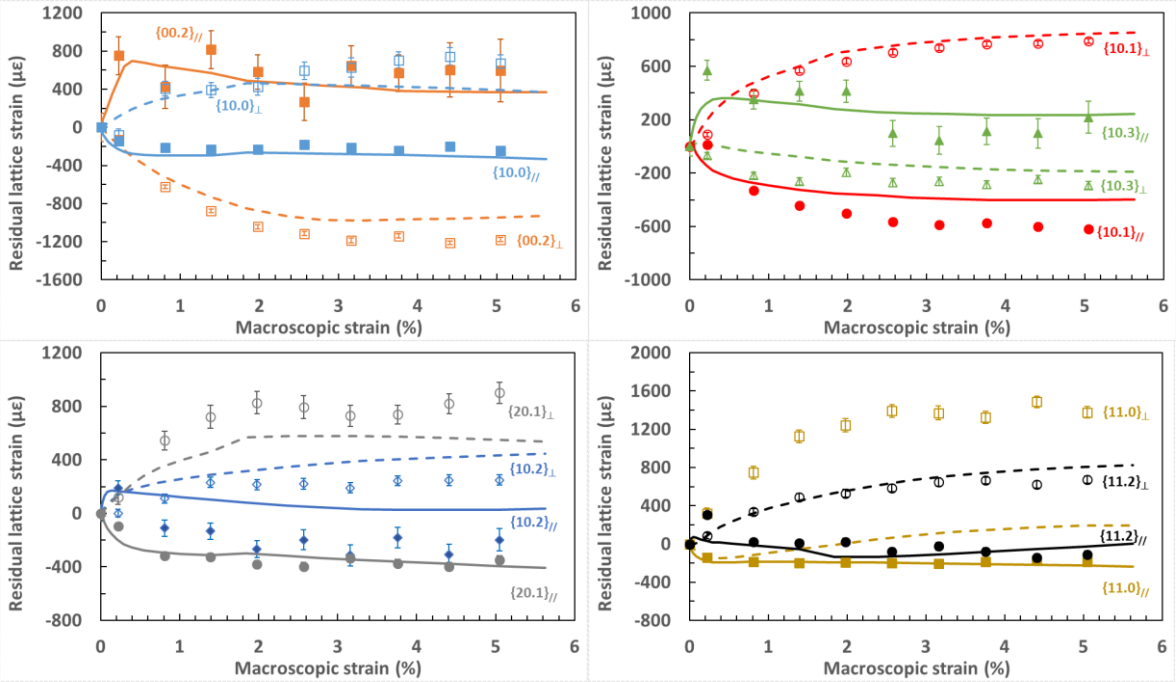

Figure 5: Experimental (symbols) and calculated (lines) residual lattice strains as a function of the macroscopic strain at RT in longitudinal (filled symbols and solid lines) and transverse (open symbols and dashed lines) directions.

The results clearly show the anisotropic mechanical behaviour of the {hk.l} grain groups. Depending on the measurement direction, the tensile or compressive behaviour of the grains participating in the {hk.l} reflection is reasonably reproduced by the simulations.

According to our simulations, at RT (Figure 5), microplasticity first initiates in the $\{10.0\}_{//}$ and $\{11.0\}_{//}$ grain groups, which are favourably oriented for the prismatic slip P⟨a⟩, at 260 MPa. The $\{20.1\}_{//}$ orientation yields at 300 MPa, highlighting the activity of the pyramidal slip $\Pi_1\langle a\rangle$. The $\{10.1\}_{//}$ and $\{10.2\}_{//}$ orientations yield at 330 MPa with the high activity of basal slip B⟨a⟩ (about 45 % of activity ratio (Figure 4.a)). The deviation from linearity of the $\{11.2\}_{//}$ grain group appears at about 330 MPa with a change in relative activity between the prismatic and basal slip (Figure 4.a). Other orientations such as $\{10.3\}_{//}$ and $\{00.2\}_{//}$ yield at 355 MPa with the activation of the pyramidal system $\Pi_1\langle c+a\rangle$ or the {11.2} twinning deformation.

Predictions at 100 °C (Figure 6) indicate that the plasticity begins with the yielding of the prismatic orientations $\{10.0\}_{//}$ and $\{11.0\}_{//}$ at 210 MPa. This behaviour matches the activity of the main deformation system i.e. the prismatic slip $P\langle a\rangle$. Plastic deformation is initiated at 234 MPa for $\{10.1\}_{//}$ grains and at 255 MPa for $\{20.1\}_{//}$ and $\{10.2\}_{//}$ orientations with the respective activation of the pyramidal $\Pi_1\langle a\rangle$ and basal $B\langle a\rangle$ systems. The $\Pi_1\langle c+a\rangle$ slip activity occurs at 300 MPa. For the $\{00.2\}_{//}$ orientation (Figure 6), a pronounced strain relief at 2.6 % total strain is observed with an experimental residual strain increasing from 243 to 1370 με. This sudden lattice strain decrease is generally observed in the case of significant twinning activity [26,30,32]. However, in our case, the monitoring of {hk.l} peak intensity and texture, which reflects twinning activity, contradicts this analysis. This reading seems consistent with the residual strain values found with the model, which report no twinning activity at this macroscopic strain. This is necessarily related to other physical phenomena that we cannot explain with the model alone.

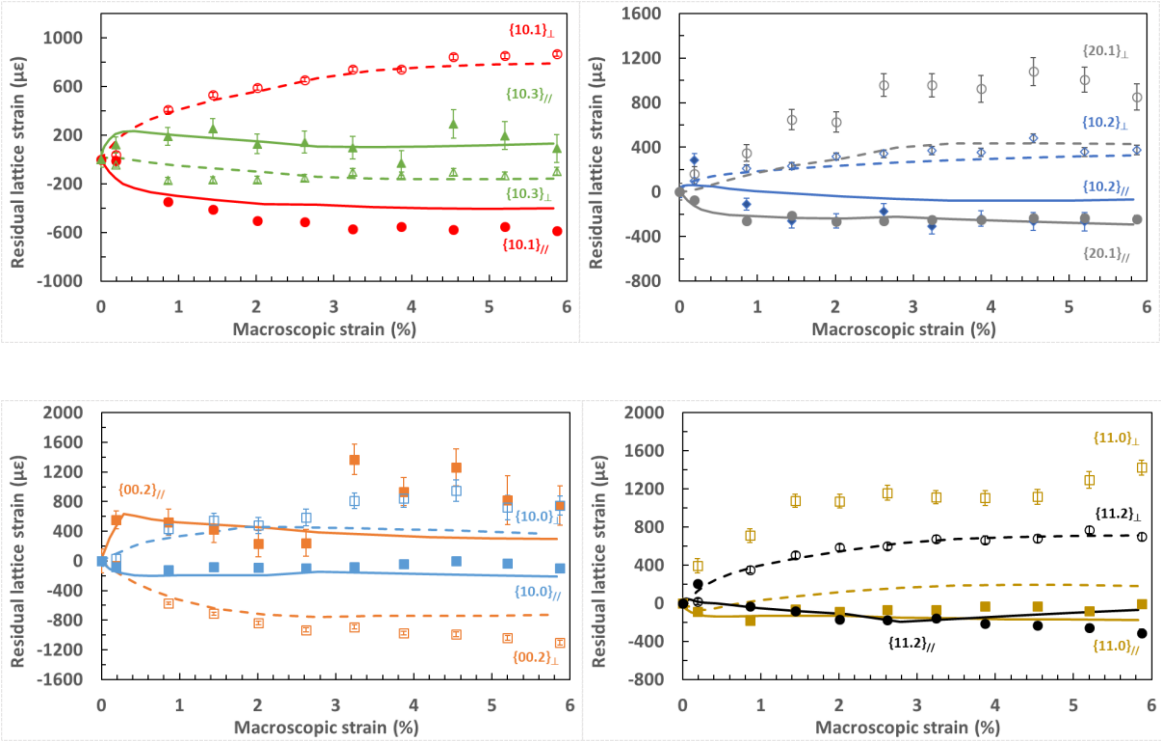

Figure 6: Experimental (symbols) and calculated (lines) residual lattice strains as a function of the macroscopic strain at 100°C in longitudinal (filled symbols and solid lines) and transverse (open symbols and dashed lines) directions.

At 300°C (Figure 7), the plasticity starts with the $\{10.0\}_{//}$ orientation, but at half the value (110 MPa) of the macroscopic stress met at 100°C (210 MPa). In particular, it can be seen that, like the macroscopic yield stress, the onset of microplasticity decreases with increasing temperature. This corresponds to the activation of the prismatic slip $P\langle a\rangle$ which has the lowest CRSS, correlated with a favourable Schmid factor for these specific {hk.l} orientations. Indeed, the grains that activate prismatic slip the first and the most easily are those whose $\vec{c}$-axis are close to 90° from the LD. With increasing applied stress, other orientations undergo plastic deformation,

e.g. $\{10.2\}_{//}$ (highlighting the activation of $B\langle a\rangle$ slip at 160 MPa) or $\{00.2\}_{//}$ (as soon as the deformation systems accommodating plasticity along the $\vec{c}$-axis become activated).

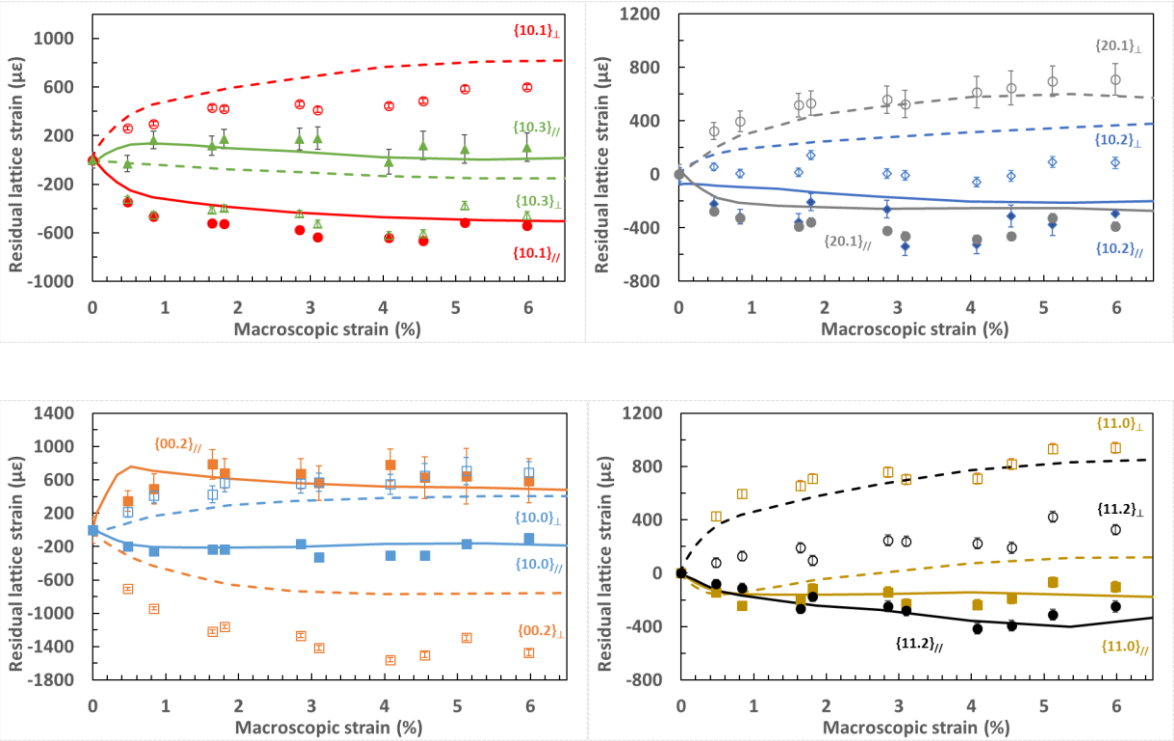

Figure 7: Experimental (symbols) and calculated (lines) residual lattice strains as a function of the macroscopic strain at 300°C in longitudinal (filled symbols and solid lines) and transverse directions (open symbols and dashed lines).

In the LD, the largest compressive strains are observed for the $\{10.0\}_{//}$, $\{20.1\}_{//}$, $\{10.2\}_{//}$ and $\{10.1\}_{//}$ plane families. It can then be assumed that these grain groups embody the plastically softest grain orientations. This is confirmed by our simulations. For example, at 5 % total strain, the experimental (resp. simulated) intergranular strain for the $\{20.1\}_{//}$ orientation is - 350 με (resp. - 392 με) at RT, - 235 με (resp. - 267 με) at 100°C and -390 με (resp. -250 με) at 300°C. In this case, the elastic tensile strains increase much less during loading due to the load transferred to other unyielded orientations.

The largest tensile strains in simulation are observed for the $\{00.2\}_{//}$ orientation at the onset of plastic deformation (696 με at RT, 634 με at 100°C and 758 με at 300°C). This highlights the load redistribution to plastically harder orientations like $\{00.2\}_{//}$ in the present case. These grains also have the highest yield stress. This is due to the fact that they are not favourably oriented for an easily activated deformation mode such as prismatic slip. A similar behaviour is observed for the $\{10.3\}_{//}$ grain group although the values of tensile strains are lower: 361 με at RT, 234 με at 100°C and 136 με at 300°C. This grain group also has an unfavourable orientation as it is relatively close to the $\{00.2\}_{//}$ orientation (Figures 5, 6 and 7). The evolution of the residual strain for the $\{00.2\}_{//}$ reflection, for all temperatures, is well described by our numerical simulations. The observed behaviour is mainly controlled by the pyramidal system $\Pi_1\langle c+a\rangle$ which accommodates plasticity along the $\vec{c}$-axis and is coupled to a lesser activation of the compressive twinning. This slip system activation explains the changes observed in the evolution of the $\{00.2\}_{//}$ residual strains that display a decrease in the measured strains after 0.4 % of total strain due to the yielding of the corresponding grains. Indeed, when the pyramidal slip $\langle c+a\rangle$ is activated, the $\{00.2\}_{//}$ grains are then favourably oriented for this mode of plastic deformation and a decrease of the intergranular elastic strain occurs. Significant deviations are however present for some cases. For example, the predicted evolution of the residual strain for the $\{10.2\}_{//}$ grain group is systematically overestimated, especially at RT, even though the model manages to correctly reproduce the general trend of this orientation for the other two temperatures. Nevertheless, the simulations provide a realistic description of the longitudinal intergranular strain evolution for the 3 temperatures and the 8 reflections selected in this study. This is particularly noteworthy as we have neglected any plastic flow in our model during the unloading steps. This assumption is less valid for the highest values of total macroscopic strain.

Despite this, the agreement between the experimental data and the numerical results remains good even for the highest macroscopic strains.

In the present study, the compressive twinning ctw-{11.2} is a secondary deformation mode. Thus, ctw-{11.2} is the mechanism which is activated last, with a contribution that decreases with increasing temperature (Figure 4). This decrease is balanced by the increase in the activity of $\langle c + a \rangle$ slip in order to accommodate the deformation along the $\vec{c}$-axis. As an example, at 3 % total strain, the contribution of the pyramidal $\Pi_1\langle c + a \rangle$ increases from 18 % at RT to about 25 % at 300°C. This is in agreement with previous work [2,15,59] where a decrease in twinning activity has been observed with increasing temperature.

In general, {hk.l} orientations which are in tension in the LD adopt a compressive behaviour in the TD, highlighting the Poisson effect. More significant deviations of the simulated results from the experimental data can be observed in the TD, especially at high temperatures (Figure 7). As an example, for the $\{11.0\}_{\perp}$ orientation at 300°C, the residual strain is underestimated. Deviations of more than 450 με can be noted above 2.3 % of total strain. A similar observation can be made for the $\{11.2\}_{\perp}$ grain group (Figure 7). Nevertheless, the model predicts the residual strain evolution for the majority of the 8 planes families studied for this measurement direction (TD), especially the $\{10.1\}_{\perp}$, $\{00.2\}_{\perp}$, $\{102\}_{\perp}$ and $\{20.1\}_{\perp}$ orientations regardless the temperature. To explain this point, it has to be noted that the $\{hk.l\}_{//}$ orientations involve only similarly oriented grains with respect to the loading direction and are thus not so sensitive to slight variations in the representation of the crystallographic texture, contrary to $\{hk.l\}_{\perp}$ grain groups. All grains with a plane-normal vector colinear to the scattering vector of the TD, for a given {hk.l} reflection, have a shared (hk.l) plane-normal perpendicular to the loading axis. The grains which contribute to the reflection display many different crystallographic orientations with

respect to the loading axis. In other words, a rotation of a grain around an axis perpendicular to the loading direction highly changes the stiffness in the tensile direction and, consequently, the strain and stress state in the grain. Different authors highlighted that this well-known discrepancies between simulations and measurements are more pronounced perpendicularly to the loading axis than in the LD [25,29,60]. A detailed explanation concerning this point has been made in a previous work [29].

Figure 8 displays the variation of predicted CRSS for the different deformation modes as a function of the temperature. The values of CRSS decrease with increasing temperature and it is consistent with the decrease in stress values required for the onset of plastic deformation (Figure 3). The evolution of CRSS can also be explained by the evolution of dislocation motion with temperature. Indeed, the plasticity of polycrystalline materials is governed by the defect displacement (or dislocations) in particular planes and along defined directions. Heating the samples during tensile testing facilitates dislocation movement. Thus, the CRSS values for slip activation decrease with temperature whatever the considered deformation mode.

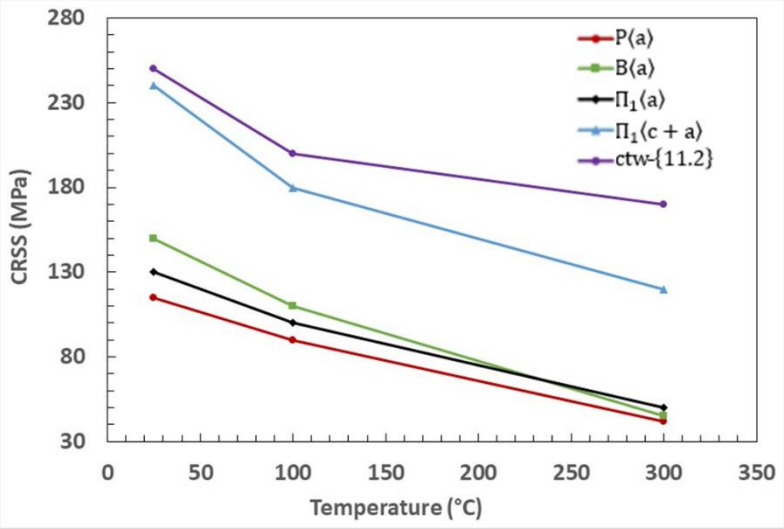

Figure 8: Evolution of CRSS for the different deformation modes as a function of temperature.

According to the simulation parameters, the ratio between the CRSS of the $P\langle a\rangle$ and basal $B\langle a\rangle$ decreases as the temperature is increasing (Table II). Such an observation has also been made by Conrad [2] on single-crystals. The slip anisotropy could be quantified by the $\frac{CRSS^{<c+a>}}{CRSS^{<a>}}$ ratio [18]. Although the slip resistance decreases for all slip systems, the $\frac{CRSS^{<c+a>}}{CRSS^{<a>}}$ ratio increases with increasing temperature. This result is consistent with the observations reported by Orozco-Caballero *et al.* [18,61] and Lütjering *et al.* [54]. The direct consequence of the increase of slip anisotropy is that the pyramidal $\Pi_1\langle c+a\rangle$ mode becomes harder to activate than $\langle a\rangle$ slip system with increasing temperature.

Conclusions

In this study, neutron diffraction results obtained on the ENGIN-X diffractometer have been compared with those obtained from a modified EPSC model. The prediction of the material (CP Ti-α) behaviour, both at the macroscopic scale and at the level of the diffracting volume, was satisfactory. It has enabled to reproduce a most of experimental evolutions in plasticity.

A parametric study was carried out in order to determine the appropriate parameter sets for the simulations at RT, 100 and 300°C. This then enabled the strong plastic anisotropy of the probed {hk.l} grain groups to be highlighted and reproduced. This study proved that the modelling should focus at the intergranular level, the scale the most sensitive to thermomechanical loading. We have shown that the stress levels required to activate the different deformation modes decrease with increasing temperature and that the contribution of these modes is sensitive to temperature. Prismatic slip remains the main mode regardless the loading temperature. The selected temperature range has revealed an evolution of the activation sequence of the slip and

twinning systems. These remarks are consistent with the studies found in the literature. We have highlighted, thanks to this coupling, an evolution in the hierarchy of the deformation modes between room temperature and 100°C, on the one hand, and 300°C, on the other hand, with an evolution between the B⟨a⟩ and Π_1⟨a⟩ systems. Furthermore, the experiment-model coupling has led to a better understanding of the development of the internal stress fields as well as the activated deformation mechanisms, despite the limitations of the model. The CRSS values chosen in our simulations have enabled to reproduce satisfactorily the behaviour of the majority of the 8 planes families for the two chosen measurement directions and for all temperatures as well as the behaviour at the macroscopic scale. It would be interesting, at this stage, to extend this study to higher temperatures to see the capacity of the model to reproduce plasticity for cases where the evolution of the hierarchy of the deformation modes would be more marked. At the same time, the development of specific hardening laws for slip/twinning systems should be introduced with a dislocation-based work-hardening law with temperature effects for a better description of the hardening process with temperature [62].

We have seen that the neutron diffraction technique is a relevant tool for the study of metallic materials, in particular for hexagonal structure, due to the different elementary mechanisms that govern their plastic behaviour. This method provides representative experimental data that can be used as a relevant tool for a more reliable modelling of the polycrystalline materials behaviour.

Acknowledgements

The authors gratefully acknowledge the ISIS Neutron Facility committee for the allocated experimental days on ENGIN-X (experiment RB171006) and GEM (experiment RB1890207) instruments, respectively.

conflict of interest statement

The authors declare that they have no conflict of interest.

References

1. P. G. Partridge, Metall. Rev. **12**, 169 (1967).

2. H. Conrad, Prog. Mater. Sci. **26**, 123 (1981).

3. F. D. Rosi, F. C. Perkins, and L. L. Seigle, JOM **8**, 115 (1956).

4. S. P. Agrawal, G. A. Sargent, and H. Conrad, Metall. Trans. **4**, 2613 (1973).

5. C. J. McHargue and J. P. Hammond, Acta Metall. **1**, 700 (1953).

6. J. C. Williams and M. J. Blackburn, Phys. Status Solidi **25**, K1 (1968).

7. A. M. Garde and R. E. Reed-Hill, Metall. Trans. **2**, 2885 (1971).

8. Y. Fu, Y. Cheng, Y. Cui, Y. Xin, Y. Zeng, X. Liu, and G. Chen, J. Mater. Sci. Technol. **126**, 237 (2022).

9. S. Nemat-Nasser, W. G. Guo, and J. Y. Cheng, Acta Mater. **47**, 3705 (1999).

10. C. P. Jiang and Z. H. Huang, Key Eng. Mater. **626**, 548 (2015).

11. N. P. Gurao, R. Kapoor, and S. Suwas, Acta Mater. **59**, 3431 (2011).

12. J. C. Williams, R. G. Baggerly, and N. E. Paton, Metall. Mater. Trans. A Phys. Metall. Mater.

Sci. **33**, 837 (2002).

13. S. Balasubramanian and L. Anand, Acta Mater. **50**, 133 (2002).

14. A. Akhtar, Metall. Trans. A **6**, 1105 (1975).

15. N. E. Paton and W. A. Backofen, Metall. Trans. **1**, 2839 (1970).

16. A. Akhtar and E. Teghtsoonian, Metall. Mater. Trans. A **6**, 2201 (1975).

17. R. E. Lim, D. C. Pagan, D. E. Boyce, J. V. Bernier, P. A. Shade, and A. D. Rollett, Mater. Charact. **174**, 110943 (2021).

18. A. Orozco-Caballero, F. Li, D. Esqué-de los Ojos, M. D. Atkinson, and J. Quinta da Fonseca, Acta Mater. **149**, 1 (2018).

19. K. Kishida, J. G. Kim, T. Nagae, and H. Inui, Acta Mater. **196**, 168 (2020).

20. V. M. Hauk and H. Behnken, in (1997).

21. A. Baczmański, Y. Zhao, E. Gadalińska, L. Le Joncour, S. Wroński, C. Braham, B. Panicaud, M. François, T. Buslaps, and K. Soloducha, Int. J. Plast. **81**, 102 (2016).

22. B. Clausen, Riso Natl. Lab. Roskilde ISBN **985**, 1 (1997).

23. R. Dakhlaoui, C. Braham, and A. Baczmański, Mater. Sci. Eng. A **444**, 6 (2007).

24. D. Gloaguen, B. Girault, J. Fajoui, V. Klosek, and M. J. Moya, Mater. Sci. Eng. A **662**, 395 (2016).

25. O. Muránsky, D. G. Carr, M. R. Barnett, E. C. Oliver, and P. Šittner, Mater. Sci. Eng. A **496**, 14 (2008).

26. F. Xu, R. A. Holt, and M. R. Daymond, Acta Mater. **56**, 3672 (2008).

27. J. L. W. Warwick, J. Coakley, S. L. Raghunathan, R. J. Talling, and D. Dye, Acta Mater. **60**, 4117 (2012).

28. A. M. Stapleton, S. L. Raghunathan, I. Bantounas, H. J. Stone, T. C. Lindley, and D. Dye, Acta Mater. **56**, 6186 (2008).

29. D. Gloaguen, G. Oum, V. Legrand, J. Fajoui, M. J. Moya, T. Pirling, and W. Kockelmann, Metall. Mater. Trans. A Phys. Metall. Mater. Sci. **46**, 5038 (2015).

30. D. Gloaguen, G. Oum, V. Legrand, J. Fajoui, and S. Branchu, Acta Mater. **61**, 5779 (2013).

31. K. E. Agbovi, B. Girault, J. Fajoui, S. Kabra, W. Kockelmann, T. Buslaps, A. Poulain, and D. Gloaguen, Mater. Sci. Eng. A **819**, 141489 (2021).

32. J. L. W. Warwick, N. G. Jones, K. M. Rahman, and D. Dye, Acta Mater. **60**, 6720 (2012).

33. J. R. Cho, D. Dye, K. T. Conlon, M. R. Daymond, and R. C. Reed, Acta Mater. **50**, 4847 (2002).

34. E. C. Oliver, M. R. Daymond, J. Quinta Da Fonseca, and P. J. Withers, J. Neutron Res. **12**, 33 (2004).

35. M. S. Lee, T. Kawasaki, T. Yamashita, S. Harjo, Y. T. Hyun, Y. Jeong, and T. S. Jun, Sci. Rep. **12**, (2022).

36. H. Li, G. Sun, W. Woo, J. Gong, B. Chen, Y. Wang, Y. Q. Fu, C. Huang, L. Xie, and S. Peng, J. Nucl. Mater. **446**, 134 (2014).

37. C. Evans, N. G. Jones, D. Rugg, T. C. Lindley, and D. Dye, J. Nucl. Mater. **424**, 123 (2012).

38. P. A. Turner and C. N. Tomé, Acta Metall. Mater. **42**, 4143 (1994).

39. B. Clausen, C. N. Tomé, D. W. Brown, and S. R. Agnew, Acta Mater. **56**, 2456 (2008).

40. L. Lutterotti, S. Matthies, H.-R. Wenk, A. S. Schultz, and J. W. Richardson, J. Appl. Phys. **81**, 594 (1997).

41. W. Kockelmann, L. C. Chapon, and P. G. Radaelli, Phys. B Condens. Matter **385-386 I**, 639 (2006).

42. A. C. Hannon, in *Nucl. Instruments Methods Phys. Res. Sect. A Accel. Spectrometers, Detect. Assoc. Equip.* (North-Holland, 2005), pp. 88–107.

43. J. R. Santisteban, M. R. Daymond, J. A. James, and L. Edwards, J. Appl. Crystallogr. **39**, 812 (2006).

44. C. M. Moreton-Smith, S. D. Johnston, and F. A. Akeroyd, J. Neutron Res. **4**, 41 (1996).

45. E. Tenckhoff, *Deformation Mechanisms, Texture, and Anisotropy in Zirconium and Zircaloy* (ASTM,Philadelphia, PA, United States, 1988).

46. D. R. Chichili, K. T. Ramesh, and K. J. Hemker, Acta Mater. **46**, 1025 (1998).

47. D. W. Brown, S. R. Agnew, M. A. M. Bourke, T. M. Holden, S. C. Vogel, and C. N. Tomé, Mater. Sci. Eng. A **399**, 1 (2005).

48. P. Lipinski and M. Berveiller, Int. J. Plast. **5**, 149 (1989).

49. G. Franz, F. Abed-Meraim, J. P. Lorrain, T. Ben Zineb, X. Lemoine, and M. Berveiller, Int. J. Plast. **25**, 205 (2009).

50. J.-P. Lorrain, T. Ben-Zineb, F. Abed-Meraim, and M. Berveiller, Int. J. Form. Process. **8**, 135 (2005).

51. D. Gloaguen, T. Berchi, E. Girard, and R. Guillén, Acta Mater. **55**, 4369 (2007).

52. C. N. Tomé, R. A. Lebensohn, and U. F. Kocks, Acta Metall. Mater. **39**, 2667 (1991).

53. P. Franciosi, M. Berveiller, and A. Zaoui, Acta Metall. **28**, 273 (1980).

54. D. Gloaguen, M. François, R. Guillen, and J. Royer, Phys. Status Solidi Appl. Res. **193**, 12 (2002).

55. E. S. Fisher and C. J. Renken, Phys. Rev. **135**, A482 (1964).

56. R. J. Wasilewski, Trans. Met. Soc. AIME **221**, (1961).

57. L. Toth and P. Van Houtte, Textures Microstruct. **19**, 229 (1992).

58. G. Simmons and H. Wang, MIT Press. Cambridge, Mass **197**, 158 (1971).

59. R. Sánchez-Martín, C. Zambaldi, M. T. Pérez-Prado, and J. M. Molina-Aldareguia, Scr. Mater. **104**, 9 (2015).

60. C. J. Neil, J. A. Wollmershauser, B. Clausen, C. N. Tomé, and S. R. Agnew, Int. J. Plast. **26**, 1772 (2010).

61. G. Lütjering and J. C. Williams, editors , in (Springer Berlin Heidelberg, Berlin, Heidelberg, 2007), pp. 15–52.

62. L. Dai and W. Song, Int. J. Plast. **154**, 103281 (2022).